Chemical Geology 662 (2024) 122192

Contents lists available at ScienceDirect

Chemical Geology

journal homepage: www.elsevier.com/locate/chemgeo

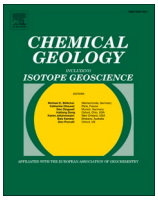

Experimental incorporation of U into xenotime at mid to lower crustal pressures and temperatures utilizing alkali-bearing fluids under reducing and oxidizing conditions

Daniel E. Harlov *

Deutsches GeoForschungsZentrum GFZ, Telegrafenberg, 14473 Potsdam, Germany

ARTICLE INFO

Editor: Claudia Romano

Keywords:
Xenotime
Uranium
HREE
Alkali-bearing fluids
Coupled dissolution-reprecipitation
Experimental petrology

ABSTRACT

A natural *gem* quality, inclusion-free, U-poor xenotime has been metasomatically altered at 900 °C and 500–1000 MPa in a series of alkali-bearing fluids including 2 N KOH, 2 N NaOH, $Na_2Si_2O_5 + H_2O$, and NaF + H_2O to which UO_2 and SiO_2 have been added. All experiments were buffered to CO_2-CO-graphite with the exception of the NaF + H_2O experiment at 900 °C and 500 MPa, which was buffered to magnetite-hematite. With the exception of the $Na_2Si_2O_5 + H_2O$ experiment, the xenotime reacted with the fluid tried in all of the remaining experiments to varying degrees. The xenotime showed the greatest degree of reactivity in the two NaF + H_2O experiments tried. This reactivity takes the form of a coupled dissolution-reprecipitation reaction, which involves enriching reacted areas of the xenotime in U + Si as well as remobilizing the HREE in these areas inherent to the original xenotime. One result was the formation of alternating bands of Y-rich and HREE- + U-rich bands in the NaF + H_2O experiment when the system was oxidized, which are presumed to have formed due a combination of simple chemical zoning coupled with diffusion and coupled dissolution-reprecipitation in the altered areas of the xenotime. A total lack of fluid and mineral inclusions on the nano-scale, as well as no disturbances in the crystal lattice in the reacted areas of the xenotime under HRTEM imaging, indicated that total recrystallization of the reacted areas took place during the course of the NaF + H_2O experiment. The results of these experiments has important implications for the metasomatic resetting of the xenotime geochromometer in the presence of alkali-bearing fluids, which would potentially allow metasomatised xenotime to time and record metasomatic events affecting the rock.

1. Introduction

After monazite, xenotime (Y,HREE,U,Th)PO_4 is one of the more relatively common accessory minerals found in igneous, metamorphic, and sedimentary rocks (Spear and Pyle, 2002; Vallini et al., 2005). In addition to being the major host for Y and the HREE, xenotime will also take in varying amounts of U and Th as the coffinite ($USiO_4$) and thorite ($ThSiO_4$) components, respectively, via the following coupled substitution reactions:

$$U^{4+} + Si^{4+} = (Y + HREE)^{3+} + P^{5+} \quad (1)$$

and

$$Th^{4+} + Si^{4+} = (Y + HREE)^{3+} + P^{5+} \quad (2)$$

(Förster, 1998) though U is preferred over Th especially in the presence of co-existing monazite ((Ce,La,Nd,LREE)PO_4) (cf. Van Emden et al., 1997; Seydoux-Guillaume et al., 2002; Förster, 1998, 2006). Compared to xenotime, monazite is a natural sink for Th via either the huttonite ($ThSiO_4$) or the cheralite ($ThCa_2O_4$) substitutions. Together, co-existing xenotime and monazite form a well calibrated geothermometer (Heinrich et al., 1997; Gratz and Heinrich, 1997, 1998) dictated in part by the amount of Y in in the monazite, i.e. an increasing Y content generally implies an increasing temperature per the relatively wide miscibility gap between the two phases. Concurrently, the Y content in garnet in the presence of co-existing xenotime has been calibrated as an empirical geothermometer for metamorphic rocks (Pyle and Spear, 1999; Pyle and Spear, 2000; Pyle et al., 2001). Because of its ability to incorporate U and Th, coupled with its relatively refractory nature, in recent years xenotime has been developed as a U-Th-Pb geochronometer (Hetherington

* Corresponding author.
E-mail address: dharlov@gfz-potsdam.de.

https://doi.org/10.1016/j.chemgeo.2024.122192
Received 1 February 2024; Received in revised form 14 May 2024; Accepted 26 May 2024
Available online 27 May 2024

et al., 2008), which has been utilized in igneous (Wang et al., 2003), metamorphic rocks (Aleinikoff and Grauch, 1990; Rasmussen et al., 2007b; Aleinikoff et al., 2015; McKinney et al., 2015), ore deposits (Rasmussen et al., 2007a; Cook et al., 2013; Zi et al., 2013; Fielding et al., 2017), and even sedimentary rocks where xenotime occurs as low temperature overgrowths on zircon (Rasmussen et al., 2004; Rasmussen, 2005; Vallini et al., 2005).

While U and Th obviously can be incorporated in xenotime during its formation via coupled substitutions (1) and (2), the question remains as to whether the U and Th can either be removed or added to xenotime during igneous processes or metamorphism. While no experimental data exists, the coupled nature of both the U and Th substitutions into the xenotime structure via Reactions (1) and (2) implies that the movement of either cation in the xenotime crystallographic lattice will also require the coupled movement of Si, which should extremely slow down the diffusion of either element through the xenotime crystallographic lattice even at high temperatures (800–900 °C) by analogy with what is seen for Th and Si (as well as Pb) in monazite (Cherniak et al., 2004; Cherniak and Pyle, 2008; Cherniak, 2010).

The goal of this study is to experimentally explore the effects that alkali-bearing fluids have on altering the U and Si content in xenotime at lower crustal P-T conditions under both reducing (C-CO_2) conditions and oxidizing (magnetite-hematite) conditions using the piston cylinder and internally heated gas pressure apparatus. The results for these experiments are then characterized, described, and interpreted using scanning electron microscopy (SEM), electron microprobe (EMP) analysis, and transmission electron microscopy (TEM).

2. Experimental and analytical procedures

2.1. Xenotime-fluid experiments

The xenotime chosen for the experiments (Table 1) consisted of a large (2 cm), semi-transparent, brownish, euhedral crystal from a pegmatite located in the Northwest Frontier Province, Pakistan (NFPP). The crystal was split into several large fragments. One fragment was crushed into 50 to 300 m size grains. Foreign mineral phases as well as cloudy grain fragments were picked out by hand and the remaining transparent, inclusion-free grain fragments washed in ethanol in an ultrasonic bath. High contrast BSE imaging and EMP analysis reveal that the NFPP xenotime grains are relatively homogeneous with respect to their (Y + HREE) content and display only faint magmatic zoning (Table 2; Fig. 1). The Th and Pb content is below the EMP detection limit whereas UO_2 ranges from 0.05 to 0.15 oxide weight percent (Table 2).

Experiments at 900 °C and 1000 MPa (Table 1) were done using a two piston cylinder apparatus as described by Johannes et al. (1971) and Johannes (1973). Each experimental charge consisted of 20 mg of xenotime plus 5 mg UO_2 and SiO_2 plus 25 to 30 mg of either 2 N KOH or 2 N NaOH, 15 mg $Na_2Si_2O_5$ + 20 mg H_2O, or 4 to 5 mg of NaF + 20 mg H_2O (Table 1). For experiments MX-97, MX-98, MX-99, and MX-107, the experimental charge was placed in a 3 mm wide, 2 cm long Au capsule, which was arc-welded shut, double folded, and placed vertically, two at a time, in a CaF_2 setup with a graphite cylindrical oven (see Fig. 3 in Harlov et al. (2011)). The thermocouple tip was placed such that it reached halfway up the side of one of the folded Au capsules. The pressure measured during the experiment was corrected for friction. Quench was achieved within 10 to 15 s by turning off the current.

The experiment at 900 °C and 500 MPa (MX-106) (Table 1) was buffered to the magnetite-hematite oxygen fugacity. Here the unfolded, 3 mm diameter, 2 cm long Pt capsule was packed with hematite + H_2O in a 5 mm diameter, 4 cm long Pt capsule, which was arc-welded shut. During the experiment the hematite reduces to magnetite thereby maintaining the buffer at $Fe_2O_3 = Fe_3O_4 + O_2$. The Pt capsule was then taken up to 900 °C and 500 MPa in an internally heated gas pressure vessel using Ar as the pressure medium. Run duration was 4 days. This was due to the amount of magnetite-hematite buffer used, which has a limited lifetime at 900 °C. The temperature was measured with 3 S-type thermocouples and calibrated based on measurements of the melting points of NaCl at 843 °C/200 MPa and 904 °C/ 500 MPa (Akella et al., 1969). The accuracy is about ±5 °C at 200 MPa and ± 20 °C at 500 MPa. Maximum thermal gradients along the capsules were ± 10 °C. Pressure measurement was done with a strain gauge and was accurate to ±7 MPa for experiments up to 500 MPa. During the experiment, pressure was controlled automatically within ±5 MPa using the hydraulic system of the intensifier and a programmable control unit. The samples were heated isobarically with a rate of 30 °C/min and quenched isobarically with quench rates of 150 to 200 °C/min. At the end of the experiment the 5 mm diameter/4 cm long Pt capsule was removed, opened and inner shiny Pt capsule removed and cleaned of buffer. The now magnetite-rich buffer remaining in the outer Pt capsule was checked to ensure that some hematite still remained, which was the case here after 4 days at 900 °C.

After each experiment, the Au (or Pt) capsule was cleaned, weighed, and punctured. The capsules were then dried at 105 °C for several hours, and weighed again to determine fluid loss. The charge was mounted in epoxy and then polished.

2.2. Scanning electron microscope (SEM) and electron microprobe (EMP) analysis

Experimental charges were first evaluated using high contrast back scattered BSE imaging on a Zeiss DSM-962 Scanning Electron

Table 1
Experimental results.

Experiment	P (MPa)	T (°C)	Time (d)	Xn (mg)	SiO_2 (mg)	UO_2 (mg)	2 N NaOH (mg)	2 N KOH (mg)	$Na_2Si_2O_5$ (mg)	NaF (mg)	H_2O (mg)	Buffer	Comments
MX-97	1000	900	7	19.78	5.12	4.88	26.13					graphite-CO_2 oxygen fugacity	partial reaction of xenotime along a few grain boundardies
MX-98	1000	900	7	20.18	4.89	5.56		25.52				graphite-CO_2 oxygen fugacity	partial reaction of xenotime along a few grain boundaries
MX-99	1000	900	7	19.65	4.92	5.18			15.25		19.95	graphite-CO_2 oxygen fugacity	no reaction observed
MX-106	500	900	4	20.29	5.49	5.67				5.25	23.72	Mt-Hm oxygen fugacity	partial to near total reaction of most of the xenotime grains
MX-107	1000	900	8	21.69	5.52	5.31				4.41	22.67	graphite-CO_2 oxygen fugacity	partial to near total reaction of most of the xenotime grains

Table 2
Representative xenotime compositions (wt%) from the xenotime metasomatism experiments.

Experiment	Description	buffer	# pts	P_2O_5	SiO_2	ThO_2	UO_2	Y_2O_3	La_2O_3	Ce_2O_3	Pr_2O_3	Nd_2O_3	Sm_2O_3	Gd_2O_3	Tb_2O_3	Dy_2O_3	Ho_2O_3	Er_2O_3	Yb_2O_3	Lu_2O_3	CaO	FeO	PbO	total
unreacted Xn	NWFP Xn		13	33.48	0.14		0.09	40.70			0.03	0.15	0.05	5.75	1.15	7.88	1.48	4.51	3.25	0.45				99.10
	std dev			*0.14*	*0.07*		*0.04*	*0.42*			*0.02*	*0.06*	*0.05*	*0.39*	*0.14*	*0.43*	*0.10*	*0.08*	*0.30*	*0.06*				
MX-97	unreacted Xn	graphite-CO_2	1	33.54	0.20	0.12	0.13	40.82			0.01	0.17	0.48	5.62	1.31	7.96	1.50	4.50	3.67	0.87	0.08	0.02		100.98
	altered Xn	graphite-CO_2	1	32.60	1.37	0.03	1.21	42.61	0.04			0.04	0.22	4.78	1.02	6.54	1.28	3.85	2.99	0.67	0.09	0.01		99.35
MX-98	unreacted Xn	graphite-CO_2	1	33.88	0.22	0.06	0.18	40.75			0.01	0.11	0.47	5.26	1.18	7.64	1.46	4.55	4.15	0.86	0.08	0.01		
	altered Xn	graphite-CO_2	1	33.73	1.07		1.83	43.31	0.01		0.02	0.03	0.27	4.20	0.91	5.92	1.19	3.70	3.05	0.70	0.06		0.02	100.02
MX-106	unreacted Xn	Mt-Hm	1	34.94	0.03	0.06	0.06	41.35	0.04		0.03	0.21	0.39	4.37	1.04	7.26	1.13	4.04	3.17	0.69	0.01			98.81
	altered Xn	Mt-Hm	1	34.34	0.36	0.02	0.59	39.66			0.01		0.21	4.62	1.04	8.30	1.38	5.01	3.15	0.70	0.02			99.40
MX-107	unreacted Xn	graphite-CO_2	1	34.87		0.10	0.08	41.32		0.02		0.13	0.57	4.51	1.08	7.42	1.12	4.10	2.98	0.75	0.01		0.02	99.09
	altered Xn	graphite-CO_2	1	33.89	0.30	0.01	0.24	38.85	0.05	0.02		0.05	0.23	4.82	1.10	8.77	1.45	5.03	3.16	0.73	0.01		0.01	98.73

blank - below the EPMA detection limit.

Fig. 1. High contrast back-scattered (BSE) image of the original unaltered NWFP xenotime grain fragments used in the experiments.

Microscope at the Deutsches GeoForschungsZentrum, Potsdam, with an accelerating voltage of 15 or 20 kV and a focused electron beam. Experimental charges were analyzed at the Deutsches GeoForschungsZentrum on a Cameca SX-100 electron microprobe operating in the wavelength dispersive mode, which is equipped with 4 crystal spectrometers and software supplied by Cameca. Individual spot analyses were made using a focused electron beam with a beam diameter of 1 μm. The accelerating voltage was 15 kV and the beam-current was 15 nA. A combination of well-characterized natural and synthetic standards were used for the calibration. These included cheralite (Th), UO_2 (U), synthetic REE phosphates prepared in Pb- and Pb-free fluxes (Y + REE) by Jarosewich and Boatner (1991), plagioclase (Si), and fluorapatite (Ca and P). The Cameca PAP correction procedure was used for all data reduction. Analytical errors for Y, the REE, Th, and other heavy elements depend on the absolute abundances of each element and the background estimation. Relative 1-σ errors were estimated to be <0.5% at the >10 wt% level, 5-10 % at the 1 wt% level, 10–20% at the 0.2 to 1 wt% level, and 20–40% at the <0.1 wt% level. For concentrations below 0.1 wt%, the analytical precision for the actinides is approximately 10% higher.

The mean EMP analysis of the starting xenotime and representative EMP analyses of the unreacted and altered xenotime for experiments MX-97, MX-98, MX-106, and MX-107 are contained in Table 2. All the EMP analyses from these experiments are listed in Supplementary Materials.

2.3. Transmission electron microscopy (TEM)

Partially altered xenotime grains, suitable for TEM investigation, were first selected using BSE and SE images. Sampling was accomplished by using focused ion beam (FIB) milling (Wirth, 2004, 2009). FIB preparation was conducted under ultra-high vacuum conditions in an oil-free vacuum system using a FEI FIB200 instrument at the GeoForschungsZentrum Potsdam. TEM-ready foils of approximately 15 × 8 × 0.15 m, representing cross sections perpendicular to and across the reaction front (separating the altered and unaltered xenotime), were sputtered directly on to the xenotime grain in the epoxy grain mount using a 30 kV Ga-ion beam. The TEM foil was protected from sputtering by the Ga-ion beam by a 1 μm thick Pt layer deposited using a high-purity organic Pt gas ($C_9H_{16}Pt$, 99.9%), which decomposes under the Ga-ion beam. Once cut, the TEM foils were placed on a perforated carbon film, which was placed on a copper grid. Carbon coating to prevent charging in the TEM was not applied.

TEM was carried out in a TECNAI F20 XTwin instrument operated at 200 kV and equipped with a FEG electron source. The TEM is equipped with a Gatan imaging filter (GIF Tridiem), a Fishione high-angle annular dark field detector (HAADF), and an EDAX X-ray analyzer with an

ultrathin window. TEM bright field, dark field, and high-resolution images (HREM) were acquired as energy-filtered images applying a 10 eV window to the zero-loss peak. Energy dispersive X-ray analysis was always performed in scanning transmission mode (STEM). The electron beam was scanned in a preselected window to reduce mass loss during measurements.

3. Experimental results

3.1. 2 N KOH, 2 N NaOH, and $Na_2Si_2O_5 + H_2O$ experiments

The 2 N KOH, 2 N NaOH, and $Na_2Si_2O_5 + H_2O$ experiments were all run at 900 °C and 1000 MPa and buffered to graphite-CO_2 (Table 1). Limited reaction textures along a few xenotime grain rims were observed for the 2 N NaOH and 2 N KOH fluid experiments (Fig. 2). In the case of the 2 N NaOH experiment (MX-97; Fig. 2a), this partly consisted of an obvious reaction rim rich in coffinite inclusions moving into the xenotime grain. The irregular outline of the reaction rim at the contact between the reacted area and the unreacted xenotime argue against it being an overgrowth. This is also seen along the reacted grain rim, which while also irregular, may or may not have experienced some overgrowth considering that coffinite grains have been incorporated into the reacted rim. In addition there are limited areas of high porosity in the reaction rim. It also resulted in limited reacted area along grain rims and cracks in the xenotime (Fig. 2b). The reacted areas are enriched in Si and U (coffinite substitution) and Y while depleted in the HREE relative to the unreacted areas (Table 2). In the 2 N KOH experiment, the reacted grains again show limited regions of alteration along the grain rim (Fig. 2c), which can be also be characterized by a dense sub-micron porosity and numerous micron to sub-micron inclusions of coffinite (Fig. 2d). Again the reacted areas are enriched in U and Si and Y while depleted in the HREE (Table 2). In the experiment involving $Na_2Si_2O_5 + H_2O$, no reaction textures were observed along any of the xenotime grain boundaries.

3.2. NaF + H_2O experiments

The NaF + H_2O experiments were both run at 900 °C but at two different oxygen fugacities and pressures (Table 1): magnetite-hematite at 500 MPa (MX-106) (Figs. 3 and 4) and graphite-CO_2 at 1000 MPa (MX-107) (Fig. 5). NaF + H_2O was chosen in part due to the fact that xenotime is relatively soluble in such solutions under high-grade conditions (Tropper et al., 2013; Mair et al., 2017) and therefore presumed to be highly reactive in such solutions. An experiment buffered to high oxygen fugacity was conducted in order to promote the presence of the considerably more mobile U^{6+} vs. the less mobile U^{4+} presumably present during the C-CO_2 metasomatism experiment. In either experiment, reaction textures enriched in U + Si were seen.

In the case of MX-106, these reaction textures are extensive and almost all the xenotime grains were affected. While some slight apparent overgrowth might be evident in the form of straight grain boundary edges, which could be interpreted as crystal faces and hence perhaps due to some overgrowth (e.g. Fig. 3a and d), the interior textures show no sign of being due to overgrowth but rather the result of a partial replacement of the original xenotime by chemically altered xenotime enriched in U via the process of coupled dissolution-reprecipitation (Putnis, 2002, 2009).

What is rather peculiar about many of these replacement textures is that they exhibit a wave-like pattern consisting of alternating concentrations and depletions of Y and the HREE (Fig. 4) such that where Y is enriched, the two HREE mapped, Dy and Er (Figs. 4c,d), are depleted and vice versa. A slight enrichment in U is also seen to out line the 'crest' of these waves where Y is depleted relative to the HREE (Fig. 4a). This pattern is also seen at the reaction front between the reacted and

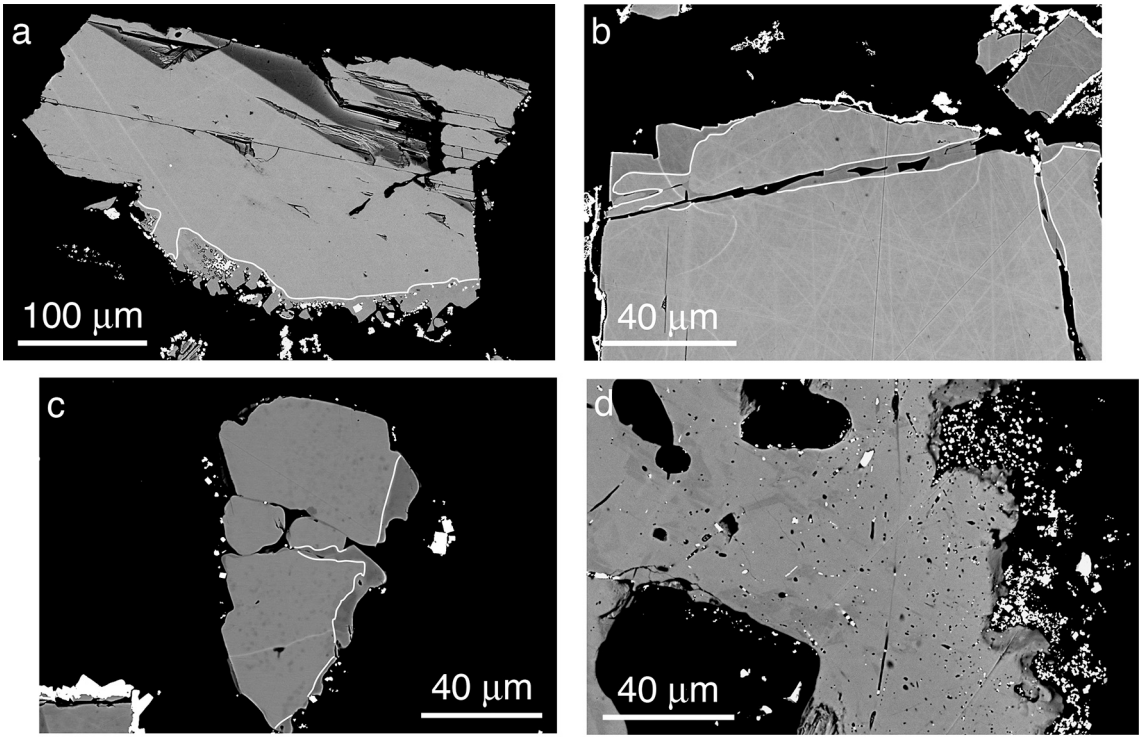

Fig. 2. High contrast BSE images of NWFP xenotime grain fragments reacted with 2 N NaOH and 2 N KOH (Table 1). The small bright inclusions and separate grains are inclusions of the mineral coffinite ($USiO_4$). Altered areas are outlined in white in Fig. 2a, b, and c. The entire area shown in Fig. 2d is altered. Fig. **2a** and **b** are shown the results of the NWFP xenotime reacted with 2 N NaOH at 900 °C and 1000 MPa and buffered to graphite-CO_2 (MX-97). In Fig. **2c** and **d**, the results from NWFP xenotime reacted with 2 N KOH at 900 °C and 1000 MPa and buffered to graphite-CO_2 (MX-98). Note the high porosity and numerous inclusions of coffinite in Fig. **2d**. Compare this texture with what is shown in in Hetherington et al. (2008), their Figs. 3, 4, and 7).

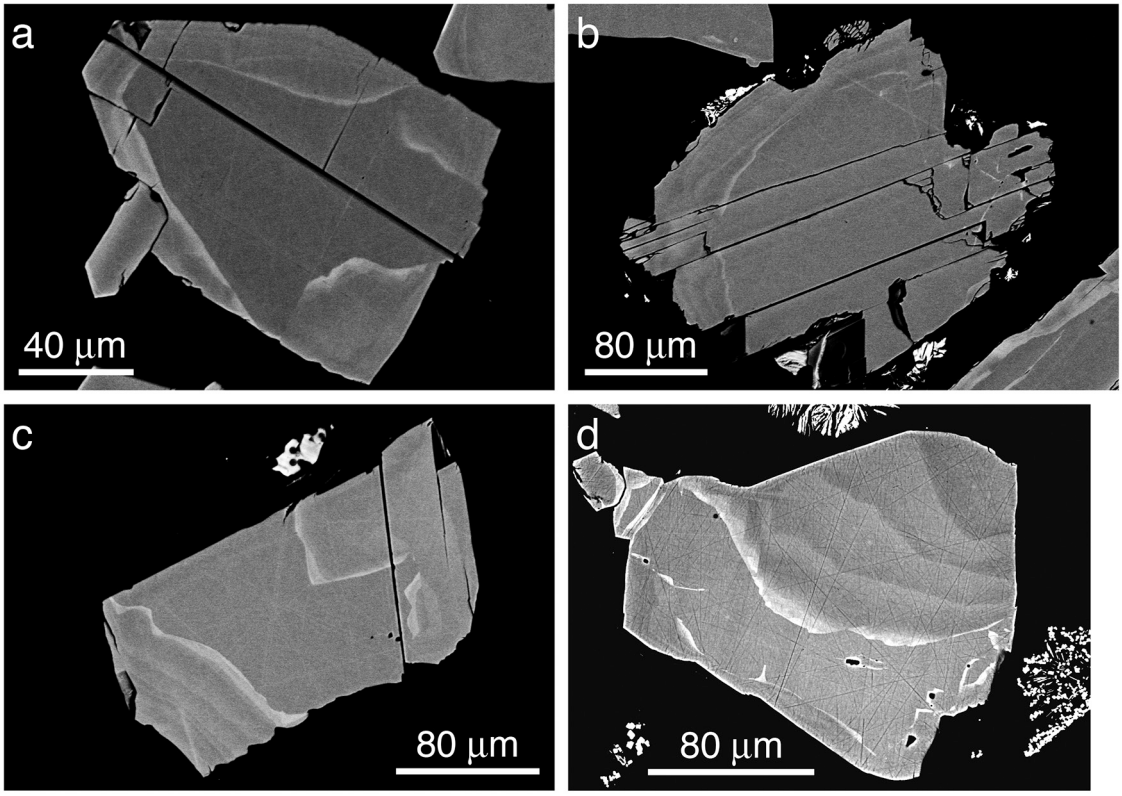

Fig. 3. High contrast BSE images of NWFP xenotime grain fragments reacted with NaF + H_2O (Table 1) buffer to magnetite-hematite oxidizing conditions at 900 °C and 500 MPa (MX-106) (Table 1). The small bright inclusions and separate grains are coffinite ($USiO_4$). Bright areas have been metasomatically altered via a coupled dissolution-reprecipitation process and are enriched in U (see Table 2 and Fig. 5). See text for a description of textures in the altered areas.

unreacted xenotime. Here enrichment in U and HREE along the reaction front is countered by depletion in Y (Fig. 4). Taking the EPMA data from the Supplementary Materials and plotting the coupled substitution $Y^{3+} + P^{5+} = Si^{4+} + U^{4+}$ (e.g. Harlov and Wirth, 2012) or the directly plotting $HREE^{3+}$ vs. Y^{3+} (where HREE = Gd, Tb, Dy, Ho, Er, and Lu) both indicate a linear relationship (see plots in the Supplementary Materials). These relationships are also brought out in the U, Dy, and Er element maps in Fig. 4.

In the case of MX-107, the reaction textures are relatively less extensive but still resemble those seen for MX-106 to some degree but with little evidence of the wave-like pattern of alternating concentrations and depletions of Y and the HREE (Fig. 5). There are some exceptions to this in the apparently slight overgrowths seen in the form of crystal faces in Fig. 5a. In general, the various alteration textures seen in MX-107 would be hard to describe as being overgrowths but again appear to be replacement textures enriched in U compared to the areas of unreacted xenotime in the same grain whose origins can be ascribed to fluid induced coupled dissolution reprecipitation (Putnis, 2002, 2009).

TEM foils extracted perpendicular to the reaction front using FIB milling (Fig. 6a) show no real evidence of a reaction front between the unreacted and reacted xenotime on the micron to submicron (nanometer) scale (Fig. 6b) compared to what has been seen in TEM foils extracted by FIB perpendicular to reaction fronts in fluorapatite (Harlov et al., 2005) and monazite (Harlov et al., 2011). From Fig. 6a, the cut of the foil indicates that at least 3/4 was taken in the reacted area of the xenotime. However, there is no apparent evidence of a reaction texture in the from of nano or micro fluid inclusions or mineral inclusions. The reacted xenotime appears to be indistinguishable from the reacted xenotime.

4. Discussion

4.1. Alteration of xenotime in U-bearing NaOH- and KOH-bearing fluids

Metasomatic alteration of xenotime from either set of experiments resulted in textures similar to that seen for metasomatised xenotime from partially metasomatically altered xenotime from the Hidra anorthosite massif, southwestern Norway (Hetherington et al., 2008). In this study the alteration textures are darker under BSE imaging compared to unaltered xenotime due to depletion of HREE and enrichment of Y, Th, and U (Table 2). The altered areas in the xenotime are characterized by numerous coffinite inclusions coupled with a high porosity indicative of metasomatic alteration, a sharp reaction front between the altered and unaltered xenotime, as well as high Y, HREE, U, and Si mobility (see Figs. 3, 4, and 7 in Hetherington et al. (2008)). These textures in natural metasomatised xenotime were interpreted by Hetherington et al. (2008) to be the result of a coupled dissolution-reprecipitation process (Putnis, 2002, 2009; Putnis et al., 2005; Putnis and Putnis, 2007; Putnis and Austrheim, 2010, 2013; Altree-Williams et al., 2015) (see below). The strong similarity with the natural xenotime would imply that the experimentally metasomatised xenotime (Fig. 2) was also altered in a coupled dissolution-reprecipitation process.

4.2. Alteration of xenotime using a NaF-bearing fluid

In a series of metasomatism experiments at 900 °C and 1000 MPa involving xenotime and the same NaF-bearing fluid used in the experiments in this study, Th was metasomatically incorporated into xenotime (Harlov and Wirth, 2012). Incorporation of Th into xenotime using NaF-bearing fluids resulted in alteration textures consisting of partial replacement of xenotime with areas enriched in Th with no real evidence of overgrowth but rather strong evidence of a coupled dissolution-

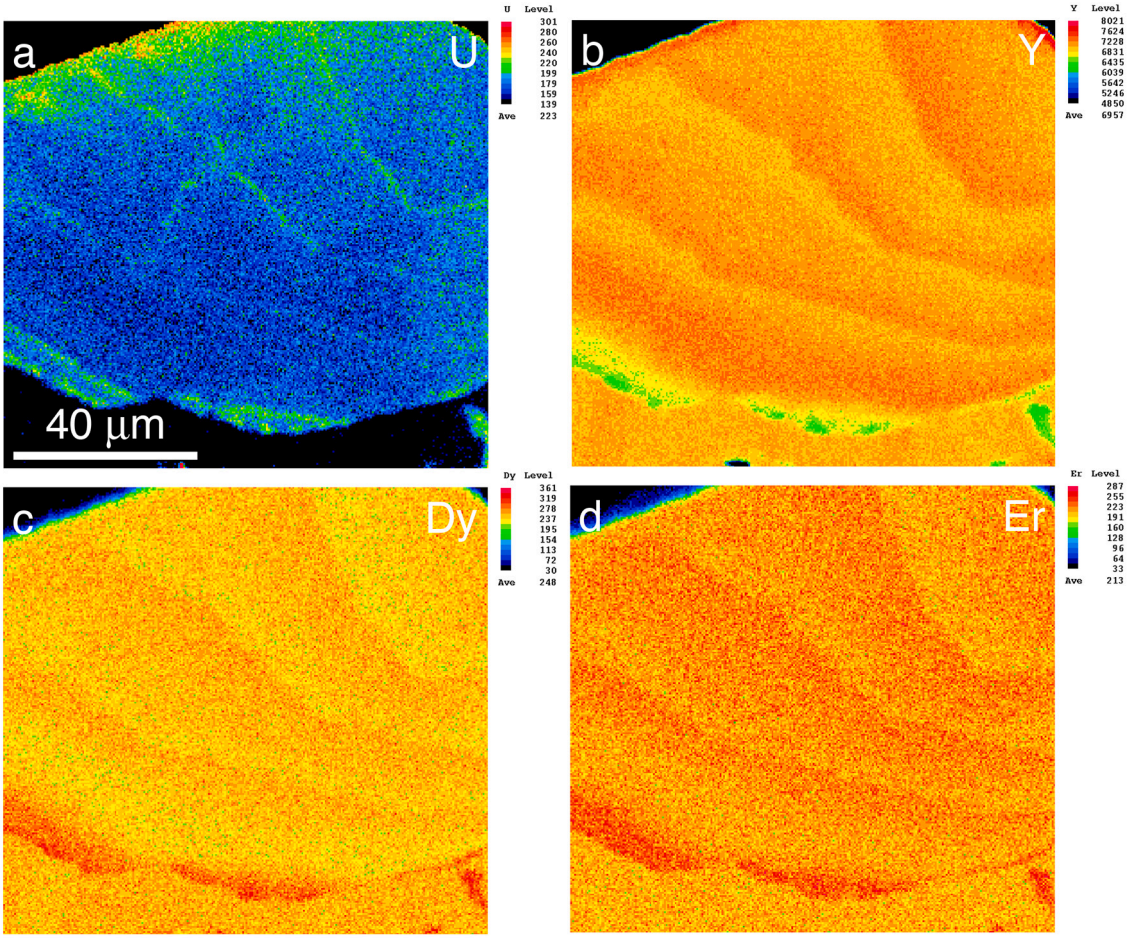

Fig. 4. U (**a**), Y (**b**), Dy (**c**), and Er (**d**) element maps of an experimentally, partially altered xenotime grain (MX-106; Table 1) show as a high contrast BSE image in Fig. 3d. See text for a description of the textures.

reprecipitation process (Putnis, 2002, 2009).

In contrast, experimental incorporation of U into xenotime utilizing the same NaF-bearing fluid, whether the experiment was buffered to either a reducing or oxidizing condition, resulted in very different textures, though a sharp contrast between the altered and unaltered xenotime is still observed (Figs. 3–5). These textures appear to be a product of both overgrowth and mineral replacement. Overgrowth is evidenced by crystal faces on some of the altered xenotime grains (Figs. 3a,d; Fig. 5a,b). As concluded for the NaOH and KOH metasomatism experiments involving xenotime, the mineral replacement textures seen here in Figs. 3 and 5 can be interpreted as a partial replacement texture due to a coupled dissolution-reprecipitation process (Putnis, 2002, 2009; Putnis et al., 2005; Putnis and Putnis, 2007; Putnis and Austrheim, 2010, 2013; Altree-Williams et al., 2015).

During coupled dissolution-reprecipitation, the original xenotime is dissolved in the presence of the NaF-bearing fluid while simultaneously being replaced by new xenotime that compositionally is in thermodynamic equilibration with the fluid chemistry under the particular P-T conditions of the system. During this process, the new xenotime uses the original xenotime as a crystallographic template for purposes of nucleation and subsequent growth/replacement. In essence, coupled dissolution-reprecipitation is the basis for mineral pseudomorphism, and is a commonly observed process in nature for many minerals. It is also the principal process by which fossilization of organic material, such as bone and wood, occurs.

In minerals, the process of coupled dissolution-reprecipitation has been shown to occur along a very thin (10 nm wide or less) fluid-filled reaction front between the original dissolving mineral and the newly growing mineral (Putnis, 2002, 2009; Altree-Williams et al., 2015). This reaction front is physically connected to the fluid surrounding the mineral grain via an actively evolving, non-static, interconnected porosity prevalent throughout the newly grown mineral phase. This allows for active, fluid-aided mass transfer between the fluid along the reaction front and the fluid surrounding the grain during the replacement process. Porosity formation can result from a variety of causes such as differences in the molar volume between the original and replacement phase or differences in solubility between the two phases (Putnis, 2009). In case of the metasomatically altered areas in the xenotime from this study, porosity formation was most likely due to chemical interaction between the fluid and the xenotime, perhaps in part due to slight differences in the solubility of the original and reacted xenotime, as opposed to a simple difference in the molar volumes of the original and reacted xenotime, considering the fact that such a difference would be quite small. Once this replacement process stops due to changing P-T-X conditions in an open fluid-mineral system or, in the case of a closed system, due to limited amounts of the reactive fluid (e.g. the experiments in this study), the reaction front will cease to advance and the altered areas of the mineral will begin to recrystallize such that the original interconnected porosity will evolve into isolated nano- and micron-size fluid inclusions often along with mineral inclusions (e.g. Fig. 2), both those genetically derived from the host mineral and those originating from minerals outside of the host mineral (Putnis, 2002, 2009; Harlov et al., 2005, 2011; Harlov and Wirth, 2012; Harlov et al., 2016).

As can be seen in Figs. 3 and 6, for each of the NaF + H_2O fluid-xenotime metasomatism experiments, neither a remnant porosity nor

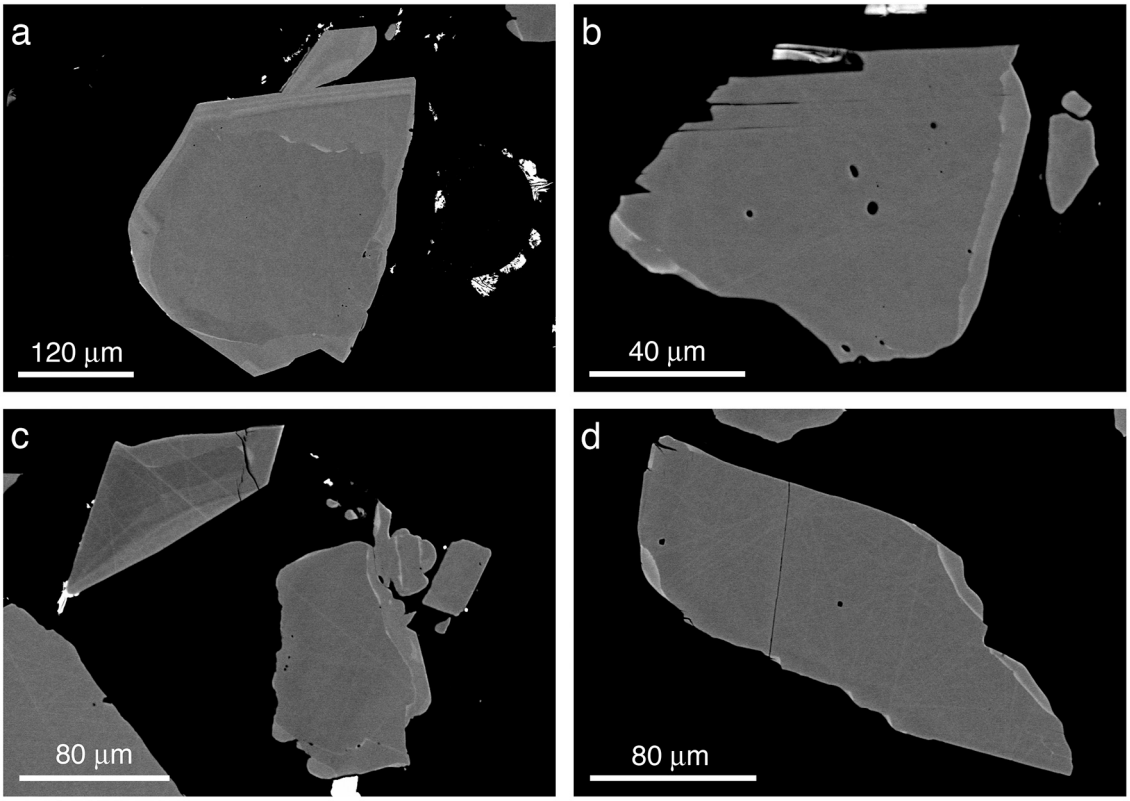

Fig. 5. High contrast BSE images of NWFP xenotime grain fragments reacted with NaF + H_2O (MX-107) conditions buffered to graphite-CO-CO_2 (Table 1). The small bright inclusions and separate grains are inclusions of the mineral coffinite ($USiO_4$). Bright areas have been metasomatically altered via a coupled dissolution-reprecipitation process and are enriched in U (see Table 2 and the Supplementary Data). See text for a description of textures in the altered areas.

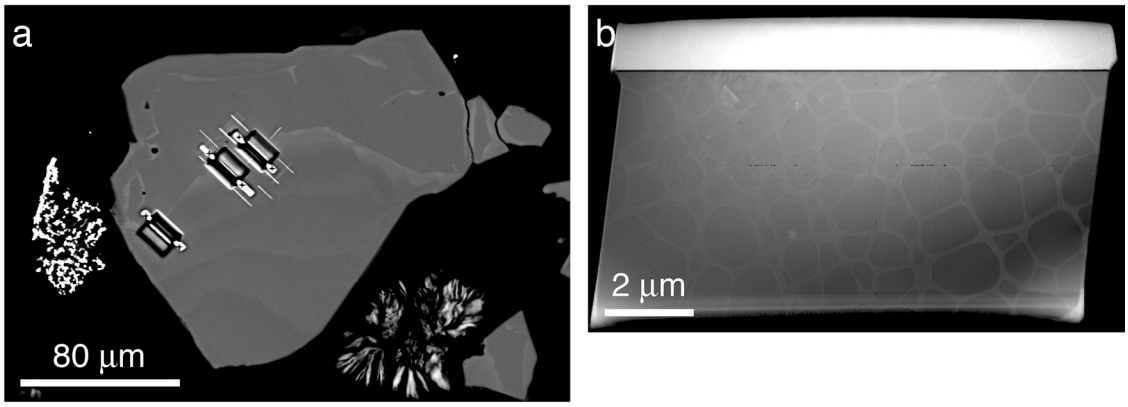

Fig. 6. Partially metasomatised xenotime grain from Figs. 3d and 4 showing location of TEM foil cuts (**6a**) taken perpendicular to the reaction front and one of the TEM foils taken (**6b**). Background honeycomb pattern is the holey carbon substrate upon which the xenotime TEM foil rests and not a structural feature of the actual TEM foil.

mineral inclusions remain in the altered areas of the xenotime under BSE imaging nor in TEM foils taken perpendicular to the reaction front, which includes both altered xenotime and unaltered xenotime (Fig. 6). Here the reaction front, so clearly visible under BSE imaging and the element maps, is not visible in the TEM foils, i.e. the altered xenotime appears texturally indistinguishable from the unaltered xenotime. This is not what is seen in the reaction textures and accompanying TEM foils taken across reaction fronts in experimentally metasomatized fluorapatite (Harlov et al., 2005) and monazite (Harlov et al., 2011) done under the same approximate P-T conditions. Here the reacted areas contain a remnant micro- and nano-porosity or fluid inclusions in addition to mineral inclusions.

Total elimination of the porosity in the reacted areas of the xenotime during the course of the NaF-fluid experiments in this study, after growth of the altered area had stopped, could be due to a rapid coarsening effect, which would be consistent with attaining textural equilibration driven by reduction in the surface area as defined by the interior surface area of the pores. Hence, the original porosity, which was transient to begin with, would have totally disappeared as textural equilibration was achieved, and in this particular case achieved rather quickly during the course of the experiment. Similar phenomena have been observed in the KBr-KCl-H_2O replacement experiments of Putnis

et al. (2005). Rapid disappearance of the porosity would have also discouraged mineral inclusion formation since the pores normally act as nucleation sites for inclusions in the altered/reacted areas (see discussion in Harlov et al., 2005).

What overgrowth that did occur was also totally recrystallized as per the above mechanism eliminating any porosity that might have formed during crystal growth outwards. The sharp compositional boundary seen between the altered xenotime and unaltered xenotime under BSE imaging and EMP element mapping would indicate that element diffusion across the reaction front was negligible at 900 °C and 1000 or 500 MPa over the course of the experiment, four and eight days, respectively (Table 1).

The formation of the alternating Y-depleted and Y-enriched zonation in the altered areas on the xenotime in MX-106 (Figs. 3c,d; Fig. 4), which was buffered to an Mt-Hm oxygen fugacity, is heavily reminiscent of mineral growth zoning in a fluid or a melt. Chemical zoning in minerals is a phenomena that has been described and interpreted for nearly 150 years staring with Rutley (1875) and Herz (1892) and continuing onwards to the present day with more recent workers (Allegre et al., 1981; Yardley et al., 1991; Jamtveit et al., 1993; Shore and Fowler, 1996; Holten et al., 2000; Kohn, 2014; see also L'Heureux, 2013). This even includes one study, which focuses on zoning in xenotime (Repina and Muftakhov, 2021). In general, these studies, and many other related studies over the last century or more, have concluded that element zoning in minerals in either magmatic or aqueous systems are a function of changes in P-T-X in the immediate vicinity of the mineral during growth, which more broadly can be due to regular and rhythmic increases and decreases in P-T, whether the system is open or not, and the depletion or enrichment of certain elements in the immediate vicinity of the mineral-fluid interface during mineral growth, including changes in the oxygen fugacity and the fugacity of other elements such as carbon, sulfur, and H_2O. Both NaF + H_2O xenotime metasomatism experiments were done in a simple closed system at a constant pressure, temperature, and oxygen fugacity, whether oxidizing or reducing, consisting only of a natural, inclusion-free, U-poor xenotime, UO_2, NaF, and H_2O (Table 1). Subsequently, in the simplest scenario, the chemical zonation with respect to U, Y and HREE seen in the altered areas, especially for the oxidized experiment (MX-106), occurred either as a product of overgrowth or partial replacement of the original xenotime via coupled dissolution-reprecipitation or else a combination of both to varying degrees (cf. Figs. 3c,d and 4).

If one assumes overgrowth, the simplest explanation for such zoning is one of relative element depletion vs. relative element enrichment at the mineral surface – fluid interface; namely in the fluid immediate to the mineral surface, Y is enriched in the mineral layer at the expense of the HREE, i.e. preferentially partitioned into the xenotime, which are thereby enriched in the fluid immediate to the mineral surface and help to form the next layer enriched in HREE compared to Y, which allows and gives time for Y to be enriched in the fluid again etc. From Fig. 4, it is also obvious to see that U followed the HREE to some degree, at least in the overall element zoning. This is especially seen at the interface between the altered and unaltered xenotime where U enrichment is strongly coupled to Y depletion and HREE enrichment again following the coupled substitution: $Y^{3+} + P^{5+} = Si^{4+} + U^{4+}$ and $HREE^{3+} + P^{5+} = Si^{4+} + U^{4+}$ (see above). The source of Y and HREE responsible for these textures would have been from the partial slight dissolution of the xenotime during the experiment.

While overgrowth is the simplest explanation, the U-enriched alteration textures seen in Figs. 3 and 4, do not appear to represent a simple overgrowth despite the formation of some crystal faces. Generally mineral overgrowth occurs uniformly or non-uniformly in a manner surrounding the entire mineral grain such that there is a core and rim structure. In general, if growth is of a free mineral grain not in contact with other grains in a fluid or melt (as is the case here), crystal faces should develop on the grain rim as it grows outward. Minerals encountered during growth will be overgrown as inclusions in the overgrowth. In contrast partial replacement via a coupled dissolution-reprecipitation process can and often occurs on only part of the grain rim most susceptible to alteration, (e.g., localized high dislocation densities, radiation damage, or other high energy disruptions in the crystal lattice), going inwards in either a lobate fashion or else following specific crystallographic planes in the mineral, though total replacement is possible. The replacement texture can be characterized by numerous small mineral inclusions and/or an evenly distributed micro- to nanoporosity. The mineral inclusions themselves can be chemically demonstrated to have originated from the host mineral by reflecting its major and/or trace element chemistry (e.g. Harlov et al., 2005).

That said, taking this explanation to the next level of complexity, namely that these alteration textures are replacement textures via a coupled dissolution-reprecipitation process, instead of growing Y- vs. HREE-enriched layers as described above, and that these layers migrate inwards into the altered xenotime, already altered by coupled dissolution-reprecipitation. This would take the form of a diffusion front moving through the fluid-filled interconnected porosity already present in a sort of chromatographic column effect with the Y, Dy, Er, and U moving in sync to each other with respect to their origin as layers on the surface of the xenotime grain where they initially formed. The end effect, other than to preserve the zoning originating on the grain surface, is to allow U, Dy, and Er to accumulate at the interface between the altered and unaltered xenotime (cf. Fig. 4). Similar behavior at the reaction interface is seen for Th in the Th-xenotime metasomatism experiments (see Figs. 2 and 5 in Harlov and Wirth, 2012) and in experiments involving metasomatism of monazite (Harlov et al., 2011), both at similar pressures and temperatures.

The fact that Y, Dy, and Er are moving in tandem with respect to each other (Fig. 4; Table 1; Supplementary Materials) may be due to the fact that they share the same approximate crystal radius on the octahedral site in xenotime (Ni et al., 1995), i.e. Y = 1.159 Å; Dy = 1.167 Å; Er = 1.144 Å, compared to the other HREE whose crystal radius is approximately 10% or more smaller (cf. Shannon, 1976). That is Y, Dy, and Er can more easily substitute for each other on the octahedral site in xenotime such that enrichment in Y means depletion in Dy and Er. In contrast, the other HREE appear to remain relatively static on the octahedral site showing little or no mobility (Table 2; Supplementary Materials). Mobility of Y, Dy, and Er is due the incorporation of U on the Y-bearing octahedral site and Si on the P site via the $U^{4+} + Si^{4+} = Y^{3+} + P^{5+}$ coupled substitution whose incorporation, while apparently resulting in Y depletion, encourages some enrichment in Dy and Er. This can be seen in Fig. 4 where regions enriched in Dy and Er are outlined by a narrow band of U enrichment as well. It can also be seen along the reaction front between the reacted and unreacted xenotime in Fig. 4 where depletion in Y is countered by relative enrichment in U, Dy, and Er.

The formation of these textures are quite pronounced for the oxidized experiment in MX-106 due to the fact that under the magnetite-hematite buffer, U would be U^{6+} as opposed to U^{4+} and thereby more mobile. This is seen when comparing MX-106 with MX-107, which was run under reducing conditions, i.e. the graphite-CO_2 buffer. Here the oxidation state of U is presumed to have been U^{4+}. In experiment MX-107, the reaction textures are considerably less extensive and less developed despite the experiment being run at the same temperature and a much higher pressure (Table 1; compare Figs. 4 and 5) for twice the amount of time as the MX-106. This would support the general conviction that U^{4+} is considerably less mobile in F-rich solutions than U^{6+}, and therefore less reactive preferring to remain as UO_2.

From the experiments involving NaF + H_2O under oxidizing conditions, the chemical zoning was obviously preserved despite the supposed inter-connected porosity completely vanishing. The only way the chemical overprint could have been changed over time would have been due to solid-state diffusion after the porosity disappeared, which in the case of xenotime is slow for HREE (Cherniak, 2010) and would be even slower for U + Si, which would have had to diffuse together at the same time in order to preserve charge balance. This is the most likely

explanation as to why the chemical overprint was preserved after the porosity vanished since when the fluid-filled porosity was present, this zoned chemical overprint must have been in some sort of equilibrium with the fluid-filled porosity and hence the porosity itself.

5. Summary and implications

Xenotime can be metasomatically altered in alkali-bearing solutions at high P-T, especially if these solutions are F-bearing. Here, utilizing these fluids, U was incorporated into the metasomatised areas of the xenotime via a coupled dissolution-reprecipitation process. This is especially seen for the NaF + H_2O experiments where U was especially mobile as U^{6+} in the oxidized experiment compared to the reduced experiment where the oxidation state of U was U^{4+} and thereby less mobile. The alternative Y and Dy + Er + U banding seen in the metasomatically altered areas of the xenotime is due to the banding originating on the surface of the xenotime and then migrating inwards into the metasomatised area via a chromatographic column affect utilizing the fluids contained in an interconnected porosity present in these areas. Dyprosium and Er move in sync with Y due to their same approximate crystal radius on the octahedral site in xenotime resulting in U + Dy + Er enrichment while Y is depleted. The results from these experiments also have implications with respect to xenotime as a geochronometer. Namely the mobility of U seen in these experiments and seen for Th in experiments involving the same alkali-bearing fluids for the same xenotime and at the same P-T conditions (Harlov and Wirth, 2012) would imply that the xenotime geochronometer could be reset in metasomatised areas of the xenotime if it encounters alkali-bearing fluids under mid to lower crustal conditions. Even though Pb mobility was not covered in these experiments, Pb probably would be mobile in these xenotime-fluid experiments based on and in analogy with the experimental results presented in Harlov et al. (2011) where monazite was metasomatically altered in alkali-bearing solutions. This would imply that xenotime, like monazite, could be used to date metasomatic events affecting the rock as a whole (see discussion in Williams et al., 2011). Lastly, while these experiments were run at 900 °C and 500–1000 MPa, this was done mostly from the standpoint of time constraints. Namely, there is no reason why the same approximate reaction textures would not form for the same experiments if run at lower temperatures and pressures if a sufficient amount of time is allowed, which is demonstrated for monazite in Harlov et al. (2011) and xenotime in Harlov and Wirth (2012). In other words, the formation of these textures in xenotime, due to metasomatic alteration, is more a function of the chemistry of the fluid as opposed to the pressure and temperature.

CRediT authorship contribution statement

Daniel E. Harlov: Writing – review & editing, Writing – original draft, Validation, Supervision, Resources, Project administration, Methodology, Investigation, Formal analysis, Data curation, Conceptualization.

Declaration of competing interest

The authors declare that they have no known competing financial interests or personal relationships that could have appeared to influence the work reported in this paper.

Data availability

One supplementary table has been uploaded with data used for this manuscript.

Acknowledgements

Dieter Rhede is thanked for his very valuable assistance on the electron microprobe with respect both to obtaining the xenotime analyses and the element map of the xenotime. Max Wilke is thanked for running experiment MX-107 at 500 MPa and 900 °C in the internally heated gas pressure vessel.

Appendix A. Supplementary data

Supplementary data to this article can be found online at https://doi.org/10.1016/j.chemgeo.2024.122192.

References

Akella, J., Vaidya, S.N., Kennedy, G.C., 1969. Melting of sodium chloride at pressures to 65 kbar. Phys. Rev. 185, 1135–1140.
Aleinikoff, J.N., Grauch, R.I., 1990. U-Pb geochronologic constraints on the origin of a unique monazite-xenotime gneiss, Hudson Highlands, NewYork. Am. J. Sci. 290, 522–546.
Aleinikoff, J.N., Lund, K., Fanning, M., 2015. SHRIMP U–Pb and REE data pertaining to the origins of xenotime in Belt Supergroup rocks: evidence for ages of deposition, hydrothermal alteration, and metamorphism. Can. J. Earth Sci. 52, 722–745.
Allegre, C.J., Provost, A., Jaupart, C., 1981. Oscillatory zoning: a pathological case of crystal growth. Nature 294, 223–228.
Altree-Williams, A., Pring, A., Ngothai, Y., Brugger, J., 2015. Textural and compositional complexities resulting from coupled dissolution–reprecipitation reactions in geomaterials. Earth Sci. Rev. 150, 628–651.
Cherniak, D.J., 2010. Diffusion in accessory minerals: zircon, titanite, apatite, monazite and xenotime. Rev. Mineral. Geochem. 72, 827–869.
Cherniak, D.J., Pyle, J.M., 2008. Th diffusion in monazite. Chem. Geol. 256, 52–61.
Cherniak, D.J., Watson, E.B., Grove, M., Harrison, T.M., 2004. Pb diffusion in monazite: a combined RBS/SIMS study. Geochim. Cosmochim. Acta 68, 829–840.
Cook, N.J., Ciobanu, C.L., O'Reilly, D., Wilson, R., Das, K., Wade, B., 2013. Mineral chemistry of rare earth element (REE) mineralization, Browns Ranges, Western Australia. Lithos 172-173, 192–213.
Fielding, I.O.H., Johnson, S.P., Zi, J.-W., Rasmussen, B., Muhling, J.R., Dunkley, D.J., Sheppard, S., Wingate, M.T.D., Rogers, J.R., 2017. Using in situ SHRIMP U-Pb monazite and xenotime geochronology to determine the age of orogenic gold mineralization: an example from the Paulsens Mine, Southern Pilbara Craton. Econ. Geol. 112, 1205–1230.
Förster, H.-J., 1998. The chemical composition of REE–Y–Th–U- rich accessory minerals from peraluminous granites of the Erzgebirge–Fichtelgebirge region, Germany. part II: xenotime. Am. Mineral. 83, 1302–1315.
Förster, H.-J., 2006. Composition and origin of intermediate solid solutions in the system thorite-xenotime-zircon-coffinite. Lithos 88, 35–55.
Gratz, R., Heinrich, W., 1997. Monazite-xenotime thermobarometry: experimental calibration of the miscibility gap in the binary system $CePO_4$-YPO_4. Am. Mineral. 82, 772–780.
Gratz, R., Heinrich, W., 1998. Monazite-xenotime thermometry. III. Experimental calibration of the partitioning of gadolinium between monazite and xenotime. Eur. J. Mineral. 10, 579–588.
Harlov, D.E., Wirth, R., 2012. Experimental incorporation of Th into xenotime at middle to lower crustal P-T utilizing alkali-bearing fluids. Am. Mineral. 97, 641–652.
Harlov, D.E., Wirth, R., Forster, H.-J., 2005. An experimental study of dissolution-reprecipitation in fluorapatite: fluid infiltration and the formation of monazite. Contrib. Mineral. Petrol. 150, 268–286.
Harlov, D.E., Wirth, R., Hetherington, C.J., 2011. Fluid-mediated partial alteration in monazite: the role of coupled dissolution–reprecipitation in element redistribution and mass transfer. Contrib. Mineral. Petrol. 162, 329–348.
Harlov, D.E., Meighan, C.J., Kerr, I.D., Samson, I.M., 2016. Mineralogy, chemistry, and fluid-aided evolution of the Pea Ridge Fe Oxide-(Y + REE) deposit, Southeast Missouri, USA. Econ. Geol. 111, 1963–1984.
Heinrich, W., Andrehs, G., Franz, G., 1997. Monazite-xenotime miscibility gap thermometry. I. An empirical calibration. J. Metamorph. Geol. 15, 3–16.
Herz, R., 1892. Über die zonarstructur der plagioklase. Tschermaks Mineral. Petrogr. Mift. 13, 343–348.
Hetherington, C.J., Jercinovic, M.J., Williams, M.L., Mahan, K., 2008. Understanding geologic processes with xenotime: composition, chronology, and a protocol for electron probe microanalysis. Chem. Geol. 254, 133–147.
Holten, T., Jamtveit, B., Meakin, P., 2000. Noise and oscillatory zoning of minerals. Geochim. Cosmochim. Acta 64, 1893–1904.
Jamtveit, B., Wogelius, R.A., Fraser, D.G., 1993. Zonation patterns of skarn garnets: records of hydrothermal system evolution. Geology 21, 113–116.
Jarosewich, E., Boatner, L.A., 1991. Rare-earth element reference samples for electron microprobe analysis. Geostand. Newslett. 15, 397–399.
Johannes, W., 1973. Eine vereinfachte Piston-Zylinder-Apparatur hoher Genauigkeit. N. Jb. Mineral. 1973, 337–351.
Johannes, W., Bell, P.M., Mao, H.K., Boettcher, A.L., Chipman, D.W., Hays, J.F., Newton, R.C., Seifert, F., 1971. An interlaboratory comparison of piston-cylinder pressure calibration using the albite-breakdown reaction. Contrib. Mineral. Petrol. 32, 24–38.
Kohn, M.J., 2014. Geochemical zoning in metamorphic minerals. In: Chapter 4. Treatise on Geochemistry, 2nd edition, pp. 249–280.

L'Heureux, I., 2013. Self-organized rhythmic patterns in geochemical systems. Phil. Trans. R. Soc. A A371, 20120356.
Mair, P., Tropper, P., Harlov, D.E., Manning, C.E., 2017. The solubility of $CePO_4$ monazite and YPO_4 xenotime in KCl-H_2O fluids at 800 °C and 1.0 GPa: implications for REE transport in high-grade crustal fluids. Am. Mineral. 102, 2457–2466.
McKinney, S.T., Cottle, J.M., Lederer, G.W., 2015. Evaluating rare earth element (REE) mineralization mechanisms in Proterozoic gneiss, Music Valley, California. Geol. Soc. Am. Bull. 127, 1135–1152.
Ni, Y., Hughes, J.M., Mariano, A.N., 1995. Crystal chemistry of the monazite and xenotime structures. Am. Mineral. 80, 21–26.
Putnis, A., 2002. Mineral replacement reactions: from macroscopic observations to microscopic mechanisms. Mineral. Mag. 66, 689–708.
Putnis, A., 2009. Mineral replacement reactions. Rev. Mineral. Geochem. 70, 87–124.
Putnis, A., Austrheim, H., 2010. Fluid-induced processes: metasomatism and metamorphism. Geofluids 10, 254–269.
Putnis, A., Austrheim, H., 2013. Mechanisms of metasomatism and metamorphism on the local mineral scale: The role of dissolution-reprecipitation during mineral reequilibration. In: Harlov, I.D.E., Austrheim, H. (Eds.), Metasomatism and the Chemical Transformation of Rock, Lecture Notes in Earth System Sciences. Springer-Verlag, Berlin Heidelberg, pp. 141–170.
Putnis, A., Putnis, C., 2007. The mechanism of re-equilibration of solids in the presence of a fluid phase. J. Solid State Chem. 180, 1783–1786.
Putnis, C.V., Tsukamoto, K., Nishimura, Y., 2005. Direct observations of pseudomorphism: compositional and textural evolution at a fluid solid interface. Am. Mineral. 90, 1909–1912.
Pyle, J.M., Spear, F.S., 1999. Yttrium zoning in garnet: coupling of major and accessory phases during metamorphic reactions. Geol. Mater. Res. 1, 1–49.
Pyle, J.M., Spear, F.S., 2000. An empirical garnet (YAG)–xenotime thermometer. Contrib. Mineral. Petrol. 138, 51–58.
Pyle, J.M., Spear, F.S., Rudnick, R.L., McDonough, W.F., 2001. Monazite-xenotime-garnet equilibrium in metapelites and a new monazite-garnet thermometer. J. Petrol. 42, 2083–2107.
Rasmussen, B., 2005. Radiometric dating of sedimentary rocks: the application of diagenetic xenotime geochronology. Earth Sci. Rev. 68, 197–243.
Rasmussen, B., Fletcher, I.R., Bengtson, S., McNaughton, N.J., 2004. SHRIMP U-Pb dating of diagenetic xenotime in the Stirling Range Formation, Western Australia: 1.8 billion year minimum age for the Stirling biota. Precambrian Res. 133, 329–337.
Rasmussen, B., Fletcher, I.R., Muhling, J.R., Thorne, W.S., Broadbent, G.C., 2007a. Prolonged history of episodic fluid flow in giant hematite ore bodies: evidence from in situ U–Pb geochronology of hydrothermal xenotime. Earth Planet. Sci. Lett. 258, 249–259.
Rasmussen, B., Fletcher, I.R., Muhling, J.R., Mueller, A.G., Hall, G.C., 2007b. Bushveld-aged fluid flow, peak metamorphism, and gold mobilization in the Witwatersrand basin, South Africa: constraints from in situ SHRIMP U-Pb dating of monazite and xenotime. Geology 35, 931–934.
Repina, S.A., Muftakhov, V.A., 2021. The nature of oscillatory zoning and mechanism of crystal growth in a paragenic intergrowth of florencite and xenotime. Geol. Ore Depos. 63, 749–771.
Rutley, F., 1875. Notes on some peculiarities in the microscopic structure of feldspars. Quart. J. Geol. Soc. London 31, 479–488.
Seydoux-Guillaume, A.-M., Wirth, R., Heinrich, W., Montel, J.-M., 2002. Experimental determination of Thorium partitioning between monazite and xenotime using analytical electron microscopy and X-ray diffraction Rietveld analysis. Eur. J. Mineral. 14, 869–878.
Shannon, R.D., 1976. Revised effective ionic radii and systematic studies of interatomie distances in halides and chaleogenides. Acta Crystallogr. A32, 751–767.
Shore, M., Fowler, A.D., 1996. Oscillatory zoning in minerals: a common phenomenon. Can. Mineral. 34, 1111–1126.
Spear, F.S., Pyle, J.M., 2002. Apatite, monazite, and xenotime in metamorphic rocks. In: Kohn, M.J., Rakovan, J., Hughes, J.M. (Eds.), Phosphates: Geochemical, Geobiological and Materials Importance, 48. Reviews in Mineralogy, Mineralogical Society of America, Washington, D.C, pp. 293–335.
Tropper, P., Manning, C.E., Harlov, D.E., 2013. Experimental determination of $CePO_4$ and YPO_4 solubilities in H_2O–NaF at 800 °C and 1 GPa: implications for rare earth element transport in high-grade metamorphic fluids. Geofluids 13, 372–380.
Vallini, D.A., Rasmussen, B., Krapez, B., Fletcher, I.R., McNaughton, N.J., 2005. Microtextures, geochemistry and geochronology of authigenic xenotime: constraining the cementation history of a Palaeoproterozoic metasedimentary sequence. Sedimentology 52, 101–122.
Van Emden, B., Thornber, M.R., Graham, J., Lincoln, F.J., 1997. The incorporation of actinides in monazite and xenotime from placer deposits in Western Australia. Can. Mineral. 35, 95–104.
Wang, R.C., Fontan, F., Chen, X.M., Hu, H., Liu, C.S., Xu, S.J., de Parseval, P., 2003. Accessory minerals in the Xihuashan Y-enriched granitic complex, southern China: a record of magmatic and hydrothermal stages of evolution. Can. Mineral. 41, 727–748.
Williams, M.L., Jercinovic, M.J., Harlov, D.E., Budzyn, B., Hetherington, C.J., 2011. Resetting monazite ages during fluid-related alteration. Chem. Geol. 283, 218–225.
Wirth, R., 2004. Focused ion beam (FIB): a novel technology for advanced application of micro-and nano-analysis in geosciences and applied mineralogy. Eur. J. Mineral. 15, 863–875.
Wirth, R., 2009. Focused Ion Beam (FIB) combined with SEM and TEM: Advanced analytical tools for studies of chemical composition, microstructure and crystal structure in geomaterials on a nanometre scale. Chem. Geol. 261, 217–229.
Yardley, B.W.D., Rochelle, C.A., Barnicoat, A.C., Lloyd, G.E., 1991. Oscillatory zoning in metamorphic minerals: an indicator of infiltration metasomatism. Mineral. Mag. 55, 357–365.
Zi, J.-W., Rasmussen, B., Muhling, J.R., Fletcher, I.R., Thorne, A.M., Johnson, S.P., Cutten, H.N., Dunkley, D.J., Korhonen, F.J., 2013. In situ U–Pb geochronology of xenotime and monazite from the Abra polymetallic deposit in the Capricorn Orogen, Australia: dating hydrothermal mineralization and fluid flow in a long-lived crustal structure. Precambrian Res. 260, 91–112.